JℝM PAPERS

Damping of solitons by coastal vegetation

Michele Mossa[1,2,†], **Diana De Padova**[1,2] **and Miguel Onorato**[3]

[1]DICATECh, Polytechnic University of Bari, Via E. Orabona 4, 70125 Bari, Italy

[2]CoNISMa, Piazzale Flaminio 9, 00196 Rome, Italy

[3]Dipartimento di Fisica and INFN, Università di Torino, Via P. Giuria 1, 10125 Torino, Italy

Mangroves are a natural defence of the coastal strip against extreme waves. Furthermore, innovative techniques of naturally based coast defence are used increasingly, according to the canons of eco-hydraulics. Therefore, it is important to correctly evaluate the transmission of waves through cylinder arrays. In the present paper, the attenuation of solitary waves propagating through an array of rigid emergent and submerged cylindrical stems on a horizontal bottom is investigated theoretically, numerically and experimentally. The results of the theoretical model are compared with the numerical simulations obtained with the smoothed particle hydrodynamics meshless Lagrangian numerical code and with experimental laboratory data. In the latter case, solitary waves were tested on a background current, in order to reproduce more realistic sea conditions, since the absence of circulation currents is very rare in the sea. The comparison confirmed the validity of the theoretical model, allowing its use for the purposes indicated above. Furthermore, the present study allowed for an evaluation of the bulk drag coefficient of the rigid stem arrays used, as a function of their density, the stem diameter, and their submergence ratio.

Key words: solitary waves, wave–structure interactions

1. Introduction

The paper presents a theoretical, numerical and experimental study to investigate the interaction between solitary waves with rigid emergent or submerged stem arrays, which simulate rigid vegetation or poles present for multiple reasons, such as, for example, mussel farming, wind farms in the ocean, and systems for guiding boats. It is widely recognized that vegetation plays a pivotal role, with a strong impact on the processes of transport and diffusion of nutrients and sediments, as well as on ecosystems and habitats, in the preservation and restoration of coastal environments, as it controls sedimentation and transport (Albayrak *et al.* 2011; Mossa & De Serio 2016; Mossa *et al.* 2017), as

† Email address for correspondence: michele.mossa@poliba.it

well as contributing to dissipating the energy of waves (Mendez & Losada 2004) and current wave flows (Hu *et al.* 2014). As shown by Kathiresan & Rajendran (2005), marshes and mangroves reduce coastal erosion by damping waves and storm surge, and riparian vegetation also enhances bank stability. Mangroves protect the coasts from erosion and disasters due to long waves. They also help to combat climate change by sequestering substantial amounts of carbon in the subsoil and their living structures. They are among the most carbon-rich tropical forests in the world. As highlighted by Gilman *et al.* (2008), mangroves are in fact threatened by climate change. The relative rise in sea level emerges as the primary risk, with numerous mangroves unable to match its pace. Particularly susceptible are those experiencing declining sediment elevation, such as mangroves of the Pacific Islands. Uncertainty persists with regard to other climate impacts. Gilman *et al.* (2008) observe that further research is imperative for assessment methodologies and indicators. Adaptation measures can mitigate losses, improve resilience, and facilitate mangrove migration. Essential aspects include coastal planning, catchment management, stressor mitigation, rehabilitation efforts, and expansion of protected areas. In this regard, the present paper contributes to the discussion. Lovelock *et al.* (2015) have highlighted the vital role of mangroves, emphasizing their ability to withstand rising sea levels by vertically accumulating sediment, thus maintaining suitable soil elevations for plant growth. However, in the Indo-Pacific, where most mangroves are located, sediment delivery decreases due to human activities such as damming of the rivers. This decline is particularly worrying given the region's expected high rates of sea level rise. Recent analysis shows that while sediment can support elevation gains that match or exceed sea level rise, at 69 % of sites, the current sea level rise outpaces soil elevation gains. A model based on field data suggests that mangrove forests in areas with low tidal ranges and limited sediment could face submersion by 2070.

Concerning the consequences of catastrophic long wave events, many studies (Dahdouh-Guebas & Koedam 1953; Mazda *et al.* 1997, 2006; Danielsen *et al.* 2005; Das & Jeffrey 2009; Marois & Mitsch 2015) have focused on the protective action of the coastline provided by mangrove forests. In fact, mangroves can effectively protect the coast from the action of wind and tidal waves (Mazda *et al.* 1997). However, dedicated studies suggest that long waves and storm surges behave differently. For example, as the height of the water from severe long waves and surges increases, the attenuation provided by mangrove forests is likely to be reduced. The long period of long waves can also influence the mitigation provided by mangroves because plants could already be damaged or displaced as the wave continues to propagate through the coastal forest.

Since the 1970s, solitary waves have been employed widely in the modelling of tsunamis, particularly in experimental and mathematical research (Yeh *et al.* 1994; Madsen, Fuhrman & Schäffer 2008). Another affirmation of this concept is also documented in Kobayashi & Lawrence (2004), in the recent NOAA Technical Memorandum (Synolakis *et al.* 2007), and in the extensive bibliography referenced by Madsen *et al.* (2008). However, a direct correlation with geophysical tsunamis has yet to be established, and there are undoubtedly discernible differences. From this perspective, and considering the limitations outlined in the previously cited studies, the current investigation pertains to solitary waves. Possible applications to the case of tsunamis, albeit on an approximate level, must take into account the limitations clearly indicated in the referenced studies.

The study of storm waves and long waves is of great significance for the strategic aspects of coastal management. In this regard, a study conducted after the 26 December 2004 tsunami in coastal villages along the south-east coast of India reiterates the importance of coastal mangrove vegetation and the characteristics of human inhabitation to protect lives
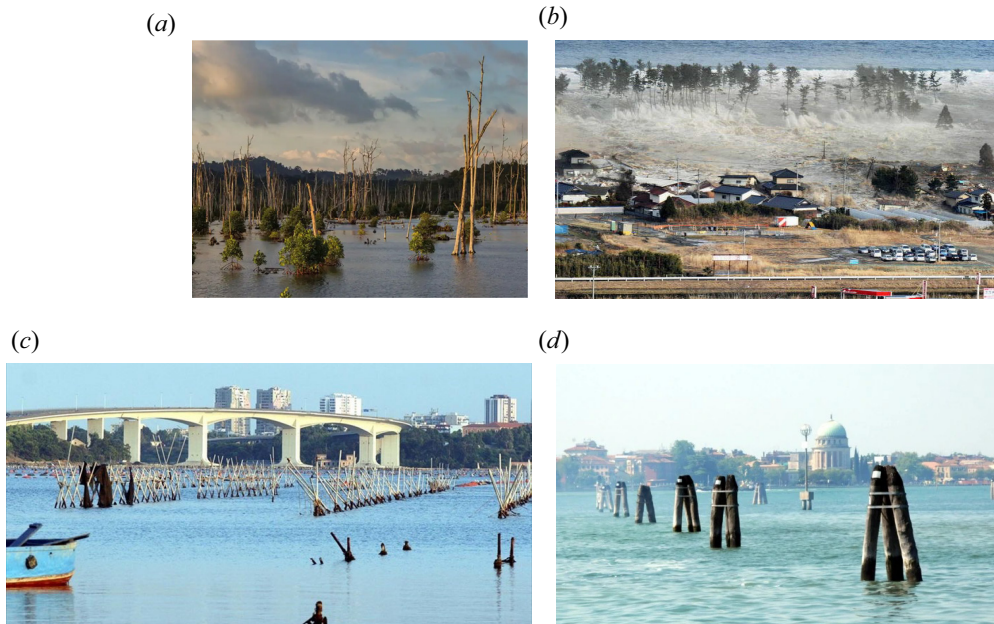
(*a*)

(*b*)

(*c*)

(*d*)

Figure 1. Example of interactions of waves and obstacles: (*a*) coastal vegetation; (*b*) Indian Ocean tsunami with coastal vegetation; (*c*) poles of a mussel farm; (*d*) typical so-called briccole of Venice.

and wealth from the fury of tsunami (Patel *et al.* 2014). In general, storm waves and long waves can cause human deaths and economic losses, which decrease with the presence of coastal vegetation, the distance from the sea, and the elevation of human habitation (Zhang & Nepf 2022). Human inhabitation should be encouraged more than 1 km from the shoreline in elevated places, behind dense mangroves and or other coastal vegetation. Some plant species are suggested, suitable to grow in between human inhabitation and the sea for coastal protection. Wetlands protect mainland areas from erosion and damage by damping waves. However, this critical role of the wetland is not fully understood at present, and a means of reliably determining the damping of the waves by vegetation in engineering practice is not yet available.

As already written, the interaction between waves and obstacles is also present for the presence of poles of mussel farms, offshore wind farms, and in other similar circumstances (Lauren, Irish & Lynett 2009; Mossa *et al.* 2021). Figure 1 shows some pictures of the possible interactions between waves and obstacles.

Mei *et al.* (2011) published a study of great interest for the analysis of emergent coastal vegetation, and Huang *et al.* (2011) analysed the interaction of solitary waves with emergent and rigid vegetation. The present study fits that context, analysing the case of solitary waves with emerged and submerged coastal vegetation.

In particular, to understand some basic mechanism of interaction between waves and structures, in the present study we consider the propagation of solitary waves through an array of cylinders. The outline of the paper is as follows. First, a theoretical model of damping of solitons – which allows us to perform a pre-evaluation of the reduction of wave heights for the dissipation of energy due to the effect of an array of cylindrical obstacles – emerged or submerged, on a horizontal bottom, is developed. The results of the theoretical model are successively compared with the numerical simulations obtained with the smoothed particle hydrodynamics (SPH) meshless Lagrangian numerical code

and with experimental laboratory data. In the latter case, solitary waves were tested on a background current, in order to reproduce more realistic sea conditions, since the absence of circulation currents is very rare in the sea. The comparison confirmed the validity of the theoretical model, allowing its use for the purposes indicated above. Furthermore, the present study allowed for an evaluation of the bulk drag coefficient of the rigid stem arrays used, as a function of their density, the diameter of the single stems, and their degree of submergence.

2. Theoretical model

2.1. *Formulation problem of the energy dissipation of solitary waves*

As is well known, a solitary wave is a self-reinforcing localized wave that maintains its shape while propagating at a constant velocity. Solitary waves are caused by cancellation of nonlinear and dispersive effects in the medium. The soliton phenomenon was first described by Russell (1845). In nature, it is difficult to form a truly solitary wave because at the trailing edge of the wave, there are usually small dispersive waves. However, long waves, such as tsunamis and waves resulting from large displacements of water due to landslides or earthquakes, behave approximately like solitary waves.

The elevation of the free surface of a solitary wave (Boussinesq 1872) is given by

$$\eta = H \operatorname{sech}^2 \left[\sqrt{\frac{3}{4} \frac{H}{h^3}} (x - Ct) \right], \tag{2.1}$$

where x is the horizontal axis, with its origin at the wave crest, t is time, h is the water depth, and H is the amplitude related to the velocity C, as (see also Daily & Stephan 1953)

$$C = \sqrt{(g(h + H))}. \tag{2.2}$$

The total energy for a solitary wave is approximately evenly divided between kinetic and potential energy. The total energy per unit width of the crest between $-x/h$ and x/h is equal to

$$\mathscr{E} = \frac{4}{3} \rho g h^2 H \left(2 + \frac{\eta}{H}\right) \left(\frac{H}{3h}\right)^{1/2} \left(1 - \frac{\eta}{H}\right)^{1/2}, \tag{2.3}$$

and the total energy per unit crest width, between $-\infty$ and $+\infty$, is

$$E = \frac{8}{3\sqrt{3}} \rho g H^{3/2} h^{3/2}. \tag{2.4}$$

As shown by Munk (1949), in the case $H/h = 0.5$, 98 % of the energy is contained between $x/h = \pm 2.1$ and, generally, a value of energy greater than 90 % is contained between $x/h = \pm 2.5$. Therefore, defining a width L_{90} that contains more than 90 % of the energy per unit crest width as

$$L_{90} = 2 \times 2.5 \times h, \tag{2.5}$$

the energy per unit area is

$$\bar{\mathscr{e}} = \frac{1}{L_{90}} \frac{4}{3} \rho g h^2 H \left(2 + \frac{\eta}{H}\right) \left(\frac{H}{3h}\right)^{1/2} \left(1 - \frac{\eta}{H}\right)^{1/2}. \tag{2.6}$$

The study relates to the propagation of solitary waves in near-shore areas where mangroves or other rigid vegetation are present. Consequently, the water depth is relatively shallow,

resulting in the group celerity coinciding with the wave celerity. Given this assumption, the energy dissipated due to the drag forces acting on the obstacle array is obtained as follows:

$$\frac{\partial \bar{\mathscr{E}} C}{\partial x} = -\epsilon_v, \tag{2.7}$$

where ϵ_v is the wave-averaged work. Equation (2.7) can be written as

$$\frac{\partial \bar{\mathscr{E}}}{\partial x} = \frac{1}{C} \left(-\epsilon_v - \bar{\mathscr{E}} \frac{\partial C}{\partial x} \right). \tag{2.8}$$

McCowan (1891) and Munk (1949) observed that the horizontal orbital velocity for a solitary wave is

$$u = C \times N \times \frac{\cosh\left(\dfrac{Mx}{h}\right)\cos\left(\dfrac{Mz}{h}\right) + 1}{\left(\cosh\left(\dfrac{Mx}{h}\right) + \cos\left(\dfrac{Mz}{h}\right)\right)^2}, \tag{2.9}$$

where z is the distance from the bottom, and M and N are functions of H/h, defined by the equations

$$\left.\begin{aligned}
\frac{H}{h} &= \frac{N}{M} \tan^{1/2}\left[M\left(1 + \frac{H}{h}\right)\right], \\
N &= \frac{2}{3} \sin^2\left[M\left(1 + \frac{2}{3}\frac{H}{h}\right)\right],
\end{aligned}\right\} \tag{2.10}$$

and shown also in figure 2.

The effect of obstructions is considered using the bulk drag coefficient C_D in the drag terms. In the following, waves propagating in an ambient flow with a regular square array of emergent or submerged cylinders of uniform diameter d and distance s will be considered. Other key parameters of the cylinder array used in the present paper are the frontal area per unit volume of the obstructions, $a = nd$, which is equal to d/s^2 in the case of a periodic square array, where n is the number of elements per unit planar area, and the stem solid volume fraction is $\phi = n\pi d^2/4$. Figure 3 shows a definition of key geometric parameters for an array of cylinders of uniform diameter d and centre-to-centre distance s.

As shown by Nepf (1999), various resistance laws of drag for flow in porous media can be derived. In particular, in free surface or atmospheric obstructed flow (White & Nepf 2007), the following quadratic form can be assumed:

$$F_D = \tfrac{1}{2}\rho \, C_D a \, |u| \, u. \tag{2.11}$$

The local variations of the velocity profiles detected in flows with obstacles are not considered here. In other terms, as proposed by Tanino & Nepf (2007) in the theoretical model, average velocity values in space are considered rather than individual point values, which can even be null at the walls of the stems impacted by the flow (see also Ben Meftah & Mossa 2016). Therefore, the enveloped cross-section velocity profile is taken into account to evaluate the effects of the presence of obstacles on the entire velocity profile, without considering the local variations upstream and downstream of the cylinders. Nor will the reflection effects of the wave with respect to each row of cylinders be considered, a situation that the literature shows has a certain importance mainly at the
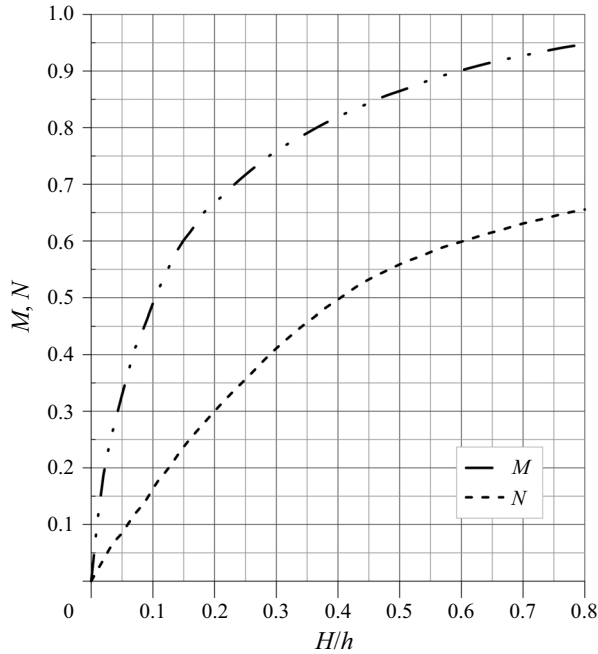
Figure 2. Functions *M* and *N* in solitary wave theory, after Munk (1949).
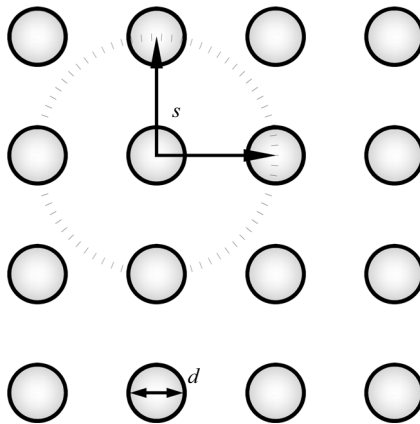

Figure 3. Definition of key geometric parameters for an array of cylinders of uniform diameter.

beginning of the stem array. Therefore, the wave dissipation evaluations will be performed starting from the wave height value starting right from the first row of cylinders. As shown by Gijón Mancheño *et al.* (2021), previous studies have highlighted that the variability of the bulk drag coefficient depends also on the processes of sheltering, which take place when downstream stem rows are exposed to the wake of upstream stem rows, resulting in a lower drag force. Sheltering under waves depends on the wavelength, which in the case in the present paper is surely greater than the stem distance. Therefore, in this paper, the sheltering effect depends only on the ratio of the stem distance and diameter.

1002 A45-6

That being said, the wave-averaged work takes the form

$$\epsilon_v = \int_0^{H+h} F_D u \, \mathrm{d}z = \int_0^{H+h} \tfrac{1}{2} \rho C_D a \, |u| \, uu \, \mathrm{d}z = \tfrac{1}{2} \rho C_D a \int_0^{H+h} |u^3| \, \mathrm{d}z. \qquad (2.12)$$

The last integral of (2.12) is

$$\int |u^3| \, \mathrm{d}z = (C \times N)^3 \times \int \left| \left(\frac{\cos\left(\dfrac{M}{h} z\right) \cosh\left(\dfrac{M}{h} x\right) + 1}{\left(\cos\left(\dfrac{M}{h} z\right) + \cosh\left(\dfrac{M}{h} x\right)\right)^2} \right)^3 \right| \mathrm{d}z. \qquad (2.13)$$

The integrand function of the equation can be expanded in a Taylor series around 0 or, in general, around z_0. These expansions are provided in the Appendix. The results of these mathematical developments indicate that the work is directly proportional to the cube of the wave celerity, and consequently the wave velocity, which is dependent on z. The solution for H/H_s is not available in closed form when applying (2.9) (McCowan 1891; Munk 1949). Therefore, the values presented in the paper are derived by applying the Taylor series expansion and then using (2.9). Although it is possible to obtain a closed-form solution for H/H_s by applying Airy's theory for small-amplitude waves, this is not possible when applying the solitary wave theory discussed in this paper. The practical steps are as follows. Evaluate the integral in (A3) to obtain (2.12), and subsequently (2.13). Equation (2.12) leads to (2.8), and ultimately, the function H is determined by (2.6).

Figure 4 shows an example of the theoretical wave heights of solitary waves propagating with obstacles on a horizontal bottom, obtained as described previously; the figure shows the results for some cases of emerged obstacles and submerged obstacles. In the latter case, as an example, the results are reported for a submergence ratio 50 %. For the simulations mentioned above, a wave height $H_s = 2$ m was assumed at the beginning of the section with obstacles, for which the longitudinal distance is $X = 0$, and at a constant depth $h = 10$ m.

The other parameters have been varied, including the submersion ratio of the obstacles, as reported in the legend of figure 4.

In the next section, the theoretical model will be validated by a comparison with numerical simulations and experimental data. The theoretical model will be used by inputting the average sea level, the wave height at the beginning of the vegetation-covered section, and an initial estimate of the bulk drag coefficient C_D. This coefficient will be adjusted until the best overlap is achieved between the wave height curves of the theoretical model and those obtained from numerical simulations and experimental data.

3. Validation of the theoretical model

3.1. *Comparison with SPH numerical solution*

The SPH method is a meshless, Lagrangian method where the fluid domain is represented by nodal points that are scattered in space with no grid structure and move with the fluid. For the sake of brevity, the full general description of the method is not reported; refer to specialized books (Liu & Liu 1998; Violeau 2012). It has proven to be applicable to a wide variety of flows, including wave breaking (Dalrymple & Rogers 2006; De Padova, Dalrymple & Mossa 2014; Makris, Memos & Krestenitis 2016), hydraulic jumps (De Padova *et al.* 2013), interaction between jets and waves (Barile *et al.* 2020), multiphase flows (De Padova *et al.* 2022), and others (Blank, Nair & Pöschel 2024). In the present
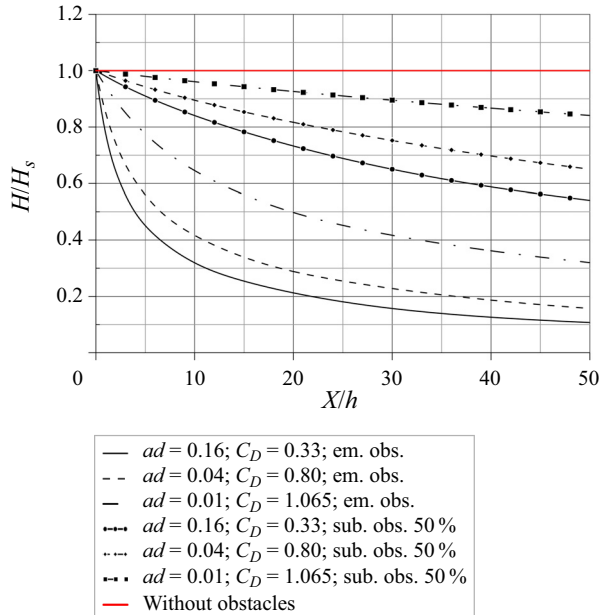
Figure 4. Theoretical wave heights of solitary waves propagating on a horizontal bottom with emerged obstacles and obstacles with a submerged ratio equal to 50 %. Here, *ad* means array density.

paper, a weakly compressible SPH model coupled with a sub-particle scale (SPS) approach to modelling turbulence (Gotoh, Shibahara & Sakai 2001) has been used. The specific features of the SPH method used here are detailed in Barile *et al.* (2020). The motion is represented by the Navier–Stokes equations for a weakly compressible fluid. In a Lagrangian frame, the equations of continuity and momentum take the form

$$\left.\begin{aligned}\frac{\mathrm{d}\rho_i}{\mathrm{d}t} &= \rho_i \sum_j \frac{m_j}{\rho_j}\left(\boldsymbol{v}_i - \boldsymbol{v}_j\right) \cdot \nabla_i W_{ij} + D_i, \\ \frac{\mathrm{d}\boldsymbol{v}_i}{\mathrm{d}t} &= -\sum_j m_j \left(\frac{P_i + P_j}{\rho_i \rho_j}\right) \nabla W_{ij} + \Gamma + \boldsymbol{g},\end{aligned}\right\} \tag{3.1}$$

where ρ is the density, $\boldsymbol{v}$ is the velocity vector, P is the pressure, D_i represents a numerical diffusive term, Γ denotes the dissipation terms, and $\boldsymbol{g}$ is the gravity acceleration vector. The summations in (3.1) are extended to all the particles j located within the circular domain centred on i and of radius $2h_{SL}$ (with h_{SL} the smoothing length), where the kernel function W_{ij} is defined. Here, the adopted kernel function W_{ij} is the cubic-spline kernel function (Monaghan & Lattanzio 1985).

In order to reduce the density fluctuation, the following numerical diffusive term D_i (Antuono, Colagrossi & Marrone 2012) is introduced:

$$D_i = \delta h c_i \sum_j \psi_{ij} \cdot \nabla W_{ij} V_j, \tag{3.2}$$

where δ is the delta-SPH coefficient, which controls the magnitude of the diffusion term, c_i is the numerical speed of sound, V_j is the associated volume of the jth particle, and ψ_{ij} is the artificial dissipation term. Here, the artificial dissipation term proposed by Molteni &
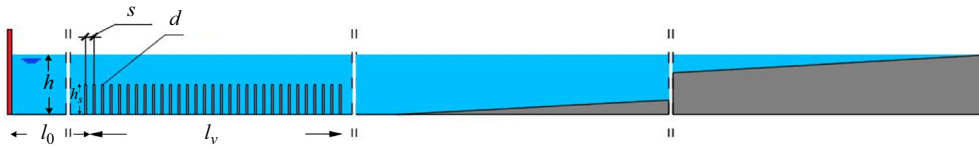
Figure 5. Front view of the computational wave tank: geometrical set-up and initial conditions.

Test	A0	A1	A2	A3	B0	B1	B2	B3	C0	C1	C2	C3
s (m)	0.12	0.12	0.12	0.12	0.10	0.10	0.10	0.10	0.08	0.08	0.08	0.08
n (cyl m^{-2})	69.44	69.44	69.44	69.44	100.00	100.00	100.00	100.00	156.25	156.25	156.25	156.25
a (m^{-1})	1.39	1.39	1.39	1.39	2.00	2.00	2.00	2.00	3.13	3.13	3.13	3.13
h_s (m)	0.50	0.45	0.35	0.25	0.50	0.45	0.35	0.25	0.50	0.45	0.35	0.25
s/d	6.0	6.0	6.0	6.0	5.0	5.0	5.0	5.0	4.0	4.0	4.0	4.0

Table 1. Values of some parameters of the numerical tests of solitary waves.

Colagrossi (1985) was chosen. The momentum dissipation term Γ is obtained by coupling the viscous dissipation in the laminar regime, as approximated by Shao & Lo (2003), with an SPS model (Fulk & Quinn 2018). A more detailed description of the large-eddy simulations SPS model using Favre averaging (Favre 1969) in a weakly compressible approach can be found in Dalrymple & Rogers (2006). The SPH results discussed here were obtained using the hardware-accelerated DualSPHysics code (Domínguez, Crespo & Gómez-Gesteira 2013). Since its first release in 2011, DualSPHysics has been shown to be robust and accurate for simulating free surface flows, but it incurs high computational cost (Crespo *et al.* 2015; Domínguez *et al.* 2021).

The numerical wave tank was 24 m long, 0.97 m high and 0.08 m wide, while the initial water depth was 0.70 m. The three-dimensional flow was simulated by discretizing the computational domain through a particle distribution with initial particle distance $Dx = Dy = Dz$ (figure 5). Starting from the wave paddle, the numerical tank has a flat bottom that extends 10 m, while the remaining bottom has slope 1/20. A vegetation canopy of length $l_x = 3$ m is housed at 4 m from the channel inlet (l_0).

Referring to previous literature, these first numerical tests have been idealized by a solitary wave (Goring 1978) passing through a group of rigid submerged cylinders with different stem distances d and different submergence ratios. The numerical simulations performed are labelled according to the stem distance s. Table 1 shows the stem height h_s for the configurations analysed. The cylinder arrays were subjected to a solitary wave with initial height (in the numerical wavemaker) $H = 0.40$ m, still-water level $h = 0.7$ m, i.e. $H/h = 0.57$, and stem diameter $d = 0.02$ m.

The validity of the selected numerical scheme was scrutinized against the solution for solitary wave elevation, specifically using (2.1) put forth by Boussinesq (1872). Keeping a constant ratio between the smoothing length and the initial particle distance ($h_{SL}/Dx = 2.5$), an investigation was carried out into the impact of the initial particle distance on the quality of the numerical result, together with a convergence analysis. For all simulations, the three-dimensional flow was modelled by discretizing the computational domain using relative particle distances $H/Dx = 20, 40, 80$ and 100, respectively. For the sake of brevity, only test A3 will be shown. As depicted in figure 6, it becomes evident that the choice of initial particle distance significantly influences the computational outcomes. In particular,
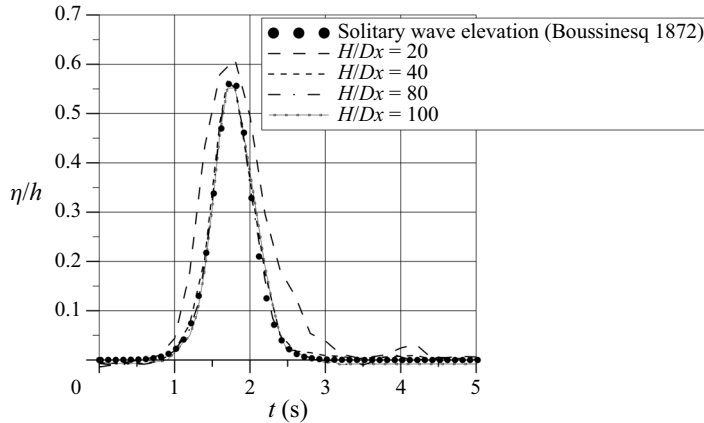
Figure 6. Effect of particle resolution on the numerical simulation (test A3): computed and analytical free surface elevation measured at a distance $x = 2.5h$; 'η' is the free surface elevation of a solitary wave.
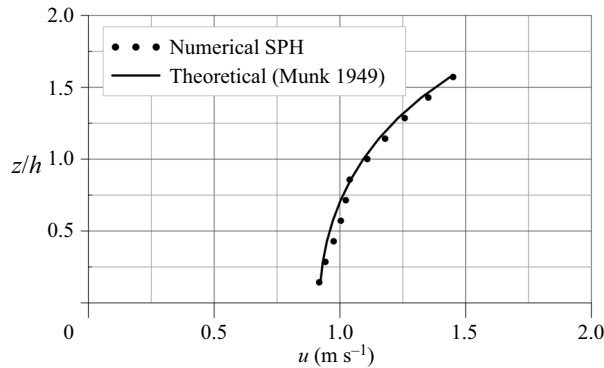

Figure 7. Comparison of the numerical and theoretical velocity profiles beneath the crest of a solitary wave (test A1 with $H/Dx = 100$).

for the case $H/Dx = 100$ with $Dx = 0.004$ m and particle count $N_p = 21\,865\,438$, there are approximately 20 particles across the width, approximately 5 particles along the stem diameter, and approximately 7 particles between the stem and the wall.

It is evident that the simulation at the lowest resolution ($H/Dx = 20$) does not accurately predict the solitary wave. Figure 6 shows that only $H/Dx \geq 40$ guarantees the independence of the SPH result from the resolution and yields a result according to the analytical solution by Boussinesq (1872). However, considering the diameter of the stem $d = 0.02$ cm and the width of the flume equal to 0.08 m, all simulations were carried out with the highest resolution $H/Dx = 100$.

Further validation of the code's numerical simulation accuracy was carried out by analysing the flow field corresponding to the well-known case in the literature of a flow impinging on a cylinder for various Reynolds numbers (results are not reported here for the sake of brevity). Furthermore, the velocity profile below the crest of a solitary wave was compared to the theoretical profile of Munk (1949). This latter result is shown in figure 7, as an example of a configuration analysed in greater detail later, demonstrating excellent agreement between the numerical and theoretical results.

The maps in figure 8, computed from the SPH vector fields in a horizontal plane at distance 0.35 m from the channel bottom, enable visualization of the degree of two-dimensionality of the vorticity. In all three configurations (A, B and C), the results show that vortex formation is due to wave action, and that the wake downstream of the single rows of stems is not sufficiently developed. Therefore, the analysed configurations are characterized by a sheltering effect due to a small value of s/d (Gijón Mancheño *et al.* 2021). At the maximum elevation of the wave over the cylinder array, where the horizontal velocity is also at its maximum, the numerical results for all three configurations (A, B and C) show clear formation of vorticity in the thin boundary layer of the cylinder. The vorticity is antisymmetric in the vertical symmetry plane of the wave tank. This pattern, observed similarly across all stems, shows negative vorticity on the left upper back side of the cylinder, and positive vorticity on the right lower side.

Figures 9–11 show a comparison of the data of dimensionless wave heights with the wave height at the beginning of the cylinder array, as functions of the longitudinal distance, non-dimensionalized with the water depth.

3.2. *Comparison with experimental results of a solitary wave superimposed on a background current*

In this subsection, the results of an experimental study of a solitary wave superimposed on a background current will be shown, to make a comparison with the proposed theoretical model. The condition of a wave superimposed on a current appears to be the most frequent in the oceans, where conditions of absence of current are quite rare. Losada, Maza & Lara (2016) presented a study evaluating the damping of regular and random waves under the combined effects of waves and both following and opposing currents. However, the particular situation that we intend to analyse will allow us to verify the ability of the theoretical model to predict the damping of solitary waves with obstacles even in the presence of a background current.

In the case of a background current propagating in the same direction as the solitary wave, the absolute celerity of the latter is given by the sum of (2.2) and the velocity of the current. The value of the background current U must also be added to the orbital velocities u. Hedges (1987) observed that, considering the component of the background current velocity in the direction of wave motion, the absolute celerity C_a – i.e. the celerity C noted by a stationary observer – is the sum of the celerity noted by an observer moving with the current (relative celerity) plus the velocity of the current U, i.e.

$$\left.\begin{aligned} C_a &= C + U, \\ u_a &= u + U. \end{aligned}\right\} \tag{3.3}$$

Therefore, in the theoretical model, (3.3) are applied, and the drag coefficient corresponds to a solitary wave when a background current is present.

However, the authors wondered whether the presence of a background current in the channel would cause variations in the solitary wave in terms of orbital velocities, wavelength and celerity. On this point, we have also considered the experimental results of solitary waves on a background channel current presented by Zhang *et al.* (2015). In this paper, the authors present experimental data regarding potential variations in celerity and wavelength in the reference frame moving with the current velocity in a channel. As already written, this is crucial to verify whether, in such a reference frame, the theory of Munk (1949) remains valid.
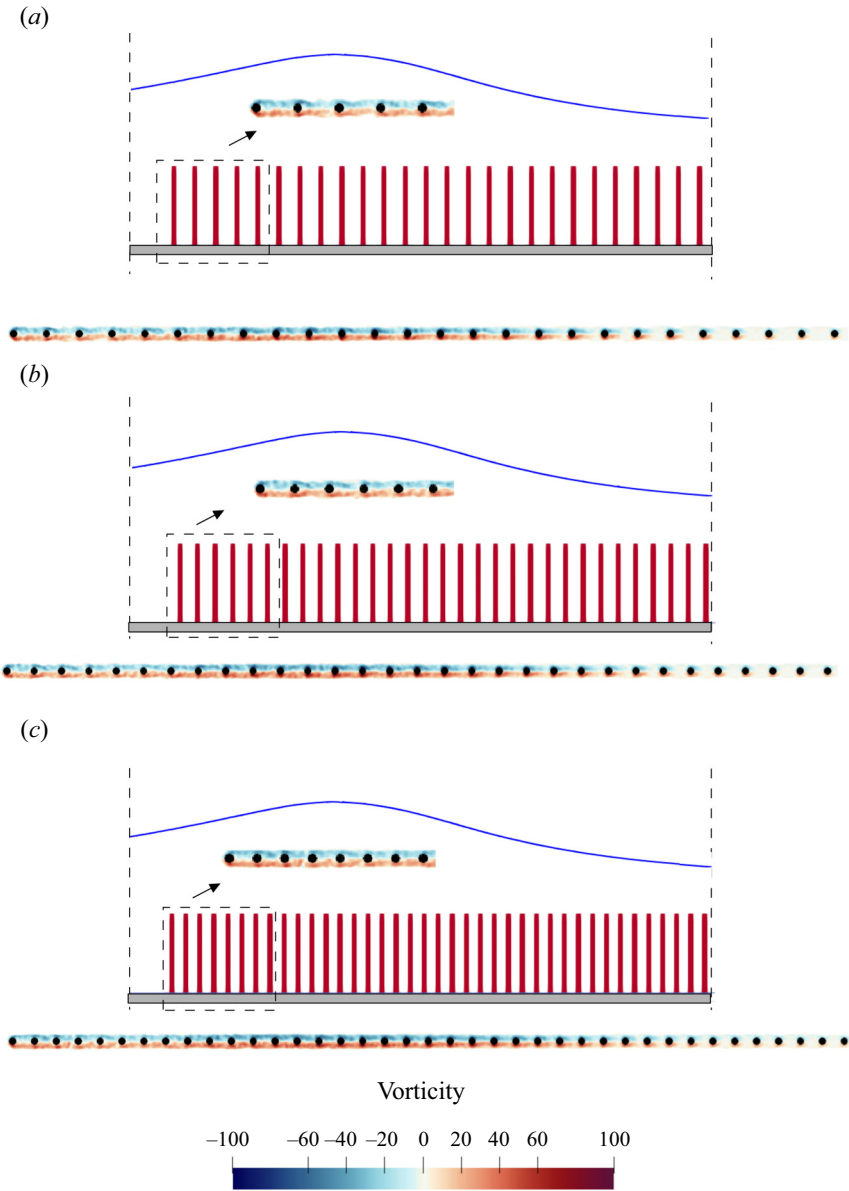
Figure 8. Vorticity (in s^{-1}) on a horizontal plane at distance 0.35 m from the channel bottom: (*a*) test A1, (*b*) test B1, (*c*) test C1.

Applying the results of Zhang *et al.* (2015) to the experimental configurations of the present paper, the wavelength, as defined by Zhang *et al.* (2015), increases by an order of magnitude of 10 %. It is important to note that Zhang *et al.* (2015) defined the characteristic wavelength as the distance between two cross-points where the horizontal line at a distance from the channel bottom equal to 20.05 m meets the surface outline of the solitary wave. Therefore, the authors' definition differs from that of Munk (1949), which, as is well known and reported in our paper, is based on the percentage of energy of the wavelength fraction. It should be noted that in our paper, in accordance with Munk (1949), we have
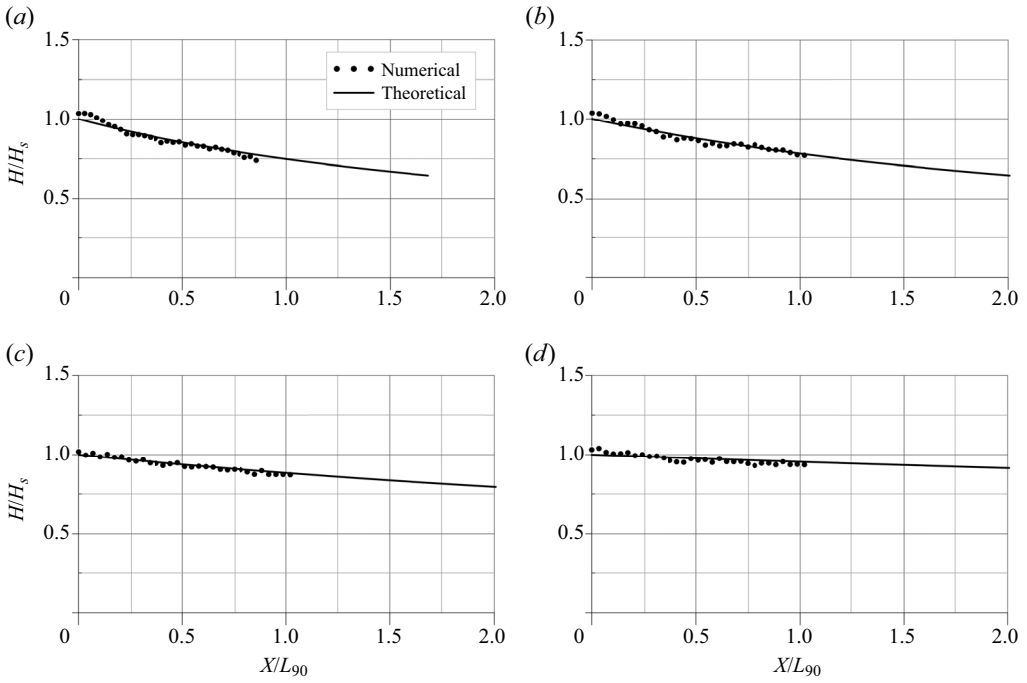
Figure 9. Comparison between theoretical and numerical wave heights of solitary waves of tests of group A: (*a*) test A0, (*b*) test A1, (*c*) test A2, (*d*) test A3.
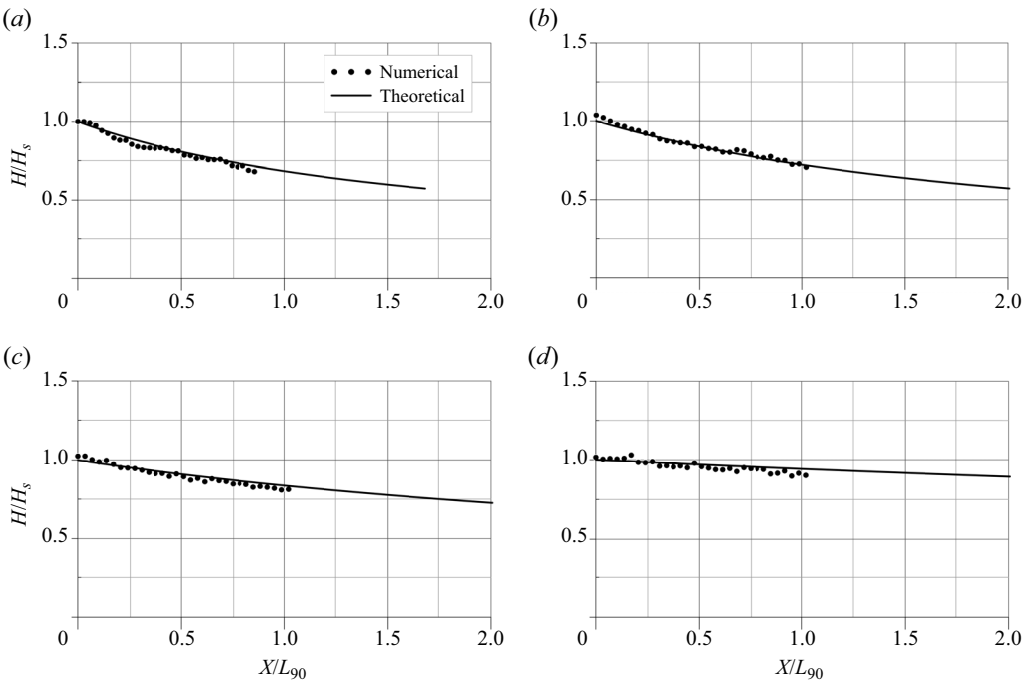

Figure 10. Comparison between theoretical and numerical wave heights of solitary waves of tests of group B: (*a*) test B0, (*b*) test B1, (*c*) test B2, (*d*) test B3.
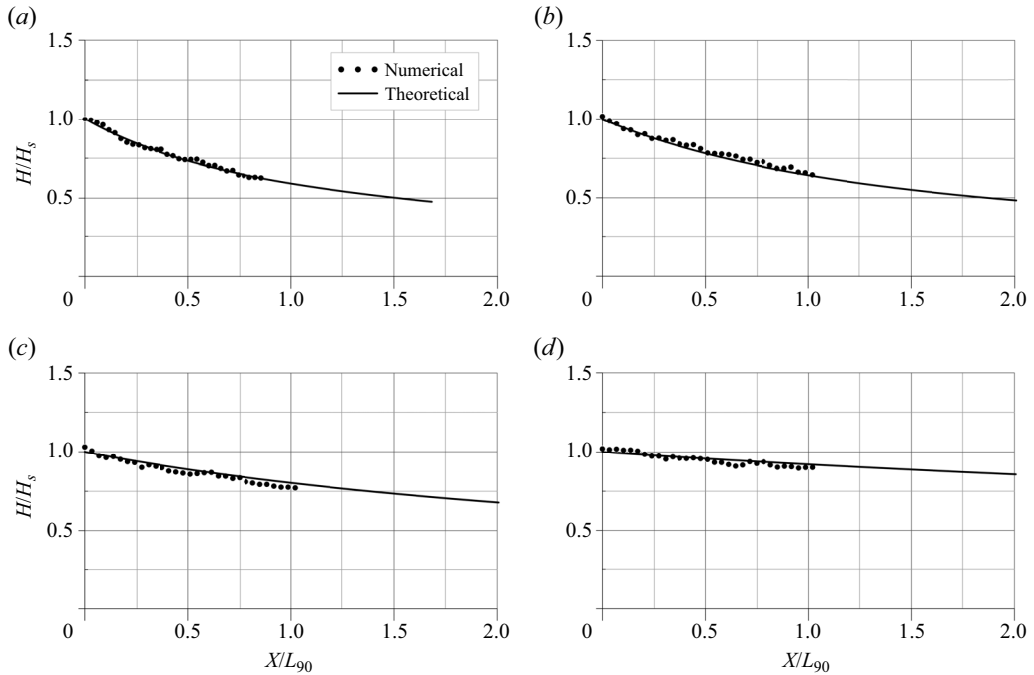
Figure 11. Comparison between theoretical and numerical wave heights of solitary waves of tests of group C: (*a*) test C0, (*b*) test C1, (*c*) test C2, (*d*) test C3.

defined L_{90} of (2.5) as a width that contains more than 90 % energy per unit width of the crest. Therefore, any increase in the length L_{90} does not contradict the definition according to which our wavelength is the one that contains 90 % or more of the wave energy. Regarding the variation of celerity, the results of Zhang *et al.* (2015) show that what was previously stated holds true, namely that in the fixed reference frame, the celerity is given by the theoretical celerity of the solitary waves plus that of the current.

In conclusion, using (3.3), since (1) the values of the wave height and the average water depth are those measured, (2) the wavelength L_{90} defined as the length that contains 90 % or more of the energy is applicable to the case of the three experimental configurations presented, and (3) the celerity in the absolute reference frame, i.e. the fixed one, is the sum of the celerity defined by Munk (1949) plus the background velocity in the channel, it is possible to apply the theoretical model with the equations of the parameters proposed in the present paper. Therefore, as mentioned earlier, the theoretical model has also been applied to the case of solitary waves with a background current.

The experiments were carried out in a rectangular flume of the Hydraulic Laboratory at the Department of Civil, Environmental, Land, Building Engineering and Chemistry (DICATECh) of the Polytechnic University of Bari, Italy (figure 12). The channel is 25 m long, 0.40 m wide and 0.50 m high, and it is made of Plexiglas to guarantee optical access.

The water recirculates through the channel in two partially separated circuits, each fed by a different tank. More precisely, the main circuit maintains steady flow conditions via a first constant head tank, whilst a secondary tank can discharge up to $0.080 \, \mathrm{m^3 \, s^{-1}}$ by regulating a software-controlled electro-valve Bellino, thus generating a wave due to the flow rate change. A triangular sharp-crested weir in the downstream tank is used to estimate the steady flow rate, while a more accurate measure of the flow rate from the secondary tank

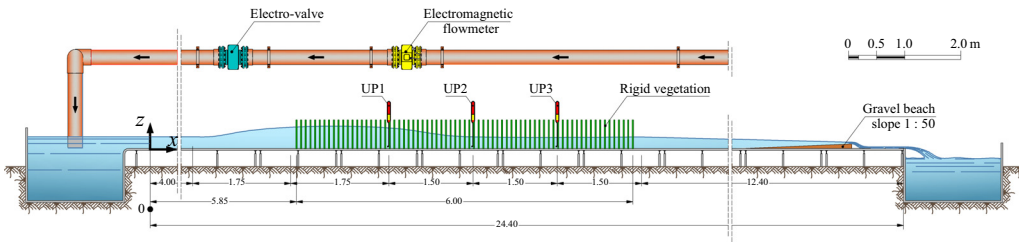Figure 12. Experimental set-up at the Polytechnic University of Bari, where UPs are the ultrasonic probes.

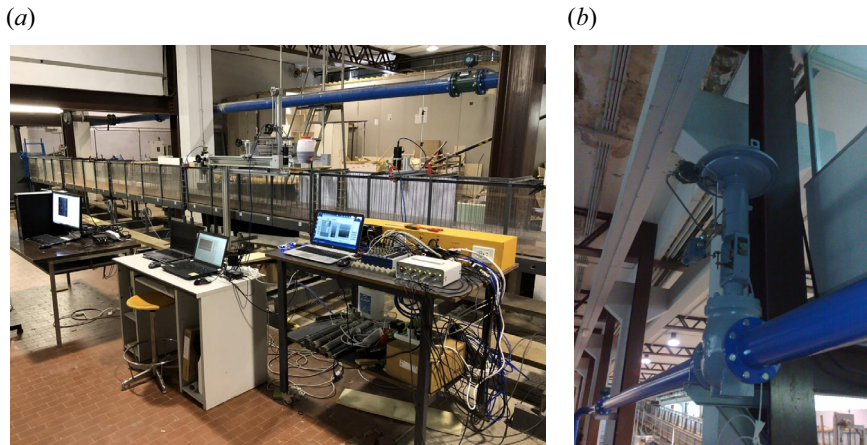(*a*)   (*b*)

Figure 13. Some photos of the complex experimental apparatus: (*a*) a view of the flume; (*b*) the electro-valve.

is provided by an electromagnetic flowmeter placed upstream of the channel. The water level of the flume was $h = 0.12$ m and was controlled by a sloping (1 : 50) gravel beach. Figure 13(*a*) shows a view of the flume section with the stem array, and figure 13(*b*) shows the electro-valve.

A six-metre-long stem array was housed within the flume at 5.85 m from the channel inlet. The stem array consists of a set of rigid steel cylinders with diameter $d = 3$ mm, inserted into six previously drilled Plexiglas panels. Three different cylinder densities and patterns are obtained using the regular grid of holes longitudinally and transversely spaced with the same axis-to-axis distance (i.e. $s = 4$ cm). As shown in figure 14, the stem patterns for the three tested configurations are characterized by a density n equal to (*a*) 156.25 cylinders m^{-2}, (*b*) 312.5 cylinders m^{-2}, and (*c*) 625 cylinders m^{-2}. Figure 15 shows a photo of the stem array, and table 2 shows the main parameters of the runs.

The free surface variation in the flume is measured by six ultrasonic probes at a 100 Hz sampling rate. The probes are located at $x = 7.50$, 9.00 and 10.50 m, so that the three sensors measure wave attenuation along the stem array (see figure 12, which includes the x, z reference coordinate system).

A solitary-like wave was generated, reaching flow peak 0.085 m^3 s^{-1}, as the sum of a steady flow 0.010 m^3 s^{-1} and an unsteady flow produced by linearly opening and closing the electro-valve for 10 s and 20 s, respectively.

Figure 16 shows a comparison between the wave height data measured and those obtained with the theoretical model. The comparison highlights the agreement between the aforementioned data even in the case of a solitary wave superimposed on a
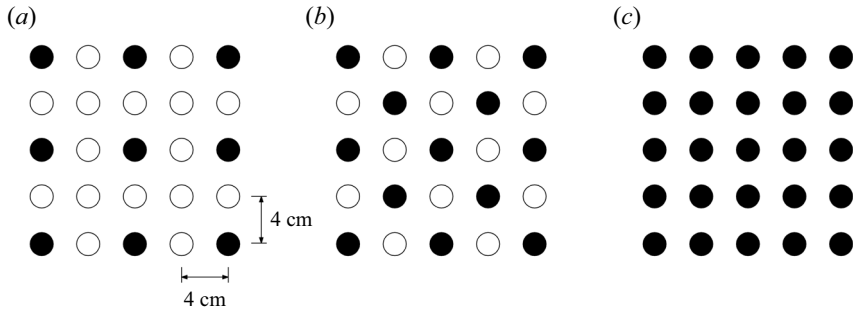
(*a*)   (*b*)   (*c*)

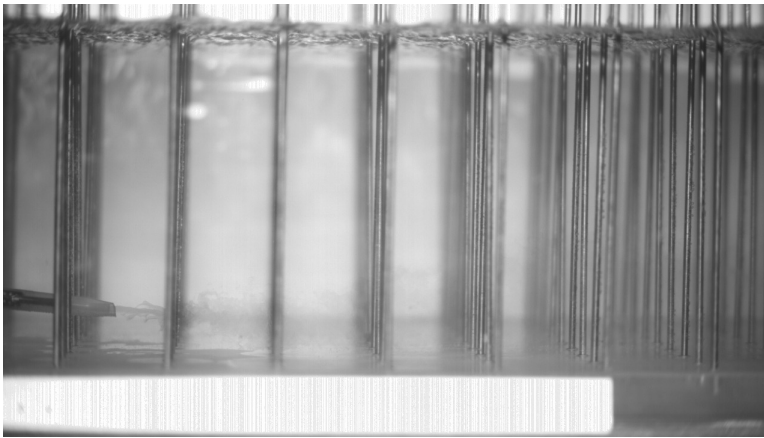Figure 14. Obstacle patterns for the three tested configurations.

Figure 15. Side view of the stem array.

Run	H_s (m)	n (cyl m^{-2})	a (m^{-1})	ad	s (m)	s/d
Exp1	0.093	156.25	0.469	0.00141	0.080	26.7
Exp2	0.099	312.50	0.937	0.00281	0.057	19.0
Exp3	0.115	625.00	1.875	0.00562	0.040	13.3

Table 2. Values of some parameters of the experimental runs of solitary waves.

background current. The measured wave damping through vegetation is the combined result of vegetation and wall friction. Even though the combined effect is expected to be greater than the wave attenuation induced by vegetation alone, the order of magnitude of wave damping caused by an array of stems is significantly higher compared to wall friction. In this regard, the experiments were conducted in a vegetated section of the channel that was sufficiently long to achieve significant wave damping but short enough for wall effects to be entirely negligible. For this purpose, reference was also made to Huang *et al.* (2011).

3.3. *The bulk drag coefficient*

Figure 17 shows the values of the bulk drag coefficients of waves analysed numerically and experimentally, and described in the previous subsections. The same figure also shows
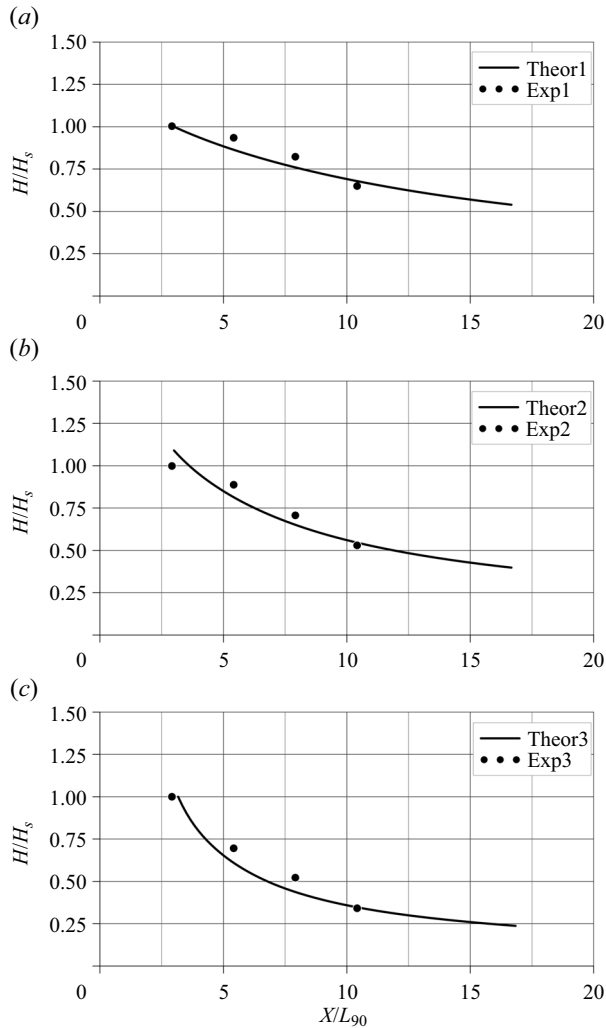
(*a*)

(*b*)

(*c*)

Figure 16. Comparison between theoretical and experimental solitary wave heights: (*a*) test Exp1, (*b*) test Exp2, (*c*) test Exp3.

the trend of the drag bulk coefficients proposed by Nepf (1999) as a function of array density *ad*, together with the range of variability of the experimental data indicated by the author. The wake interference model of Nepf (1999) predicts that the bulk drag coefficient C_D decreases with increasing *ad* for random and staggered arrays. As highlighted in the original diagram by Nepf (1999), the experimental data show a certain scatter with respect to the line shown in figure 17.

The results for the bulk drag coefficients obtained in this study are in good agreement with those reported by Nepf (1999), even when considering the fact that the latter's data pertain to a steady flow condition. This conclusion holds both for the case of waves alone and for waves superimposed on a background current. The bulk drag coefficient of the experimental configurations tends to be smaller than those identified by the curve in figure 17, even though it is in the range of the error bars of that curve. As indicated in § 2.1, high sheltering, linked to a lower value of s/d, involves a reduction in the drag force,
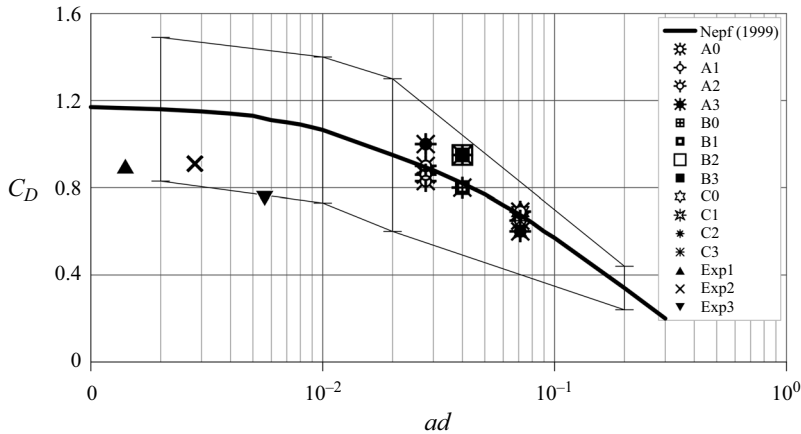
Figure 17. Diagram of the experimental values of the bulk drag coefficient C_D with the fitting line and the variability range of the experimental data from the literature (Nepf 1999).

due to the fact that downstream cylinders can be placed in the wakes of upstream elements. Even if the dimensionless distances s/d for the three experimental runs are greater than for the numerical configurations (see the comparison of the values of the parameter s/d in tables 1 and 2), the presence of a background current in the experimental tests creates a certainly more effective wake, resulting in a smaller drag force. Nevertheless, in the case of solitary waves with a background current, the experimental data for C_D confirm the trend known from the literature, whereby for values $ad < 0.001$, the value of C_D is, on average, constant.

Gijón Mancheño *et al.* (2021) also showed a dependence of the bulk drag coefficient as a function of the Keulegan–Carpenter number (Keulegan & Carpenter 1958), defined as the ratio between the drag and the inertia forces, given by the ratio between the horizontal excursion of the orbital movement of the water particles in the presence of wave motion and the diameter of the stems. The dependence of C_D on the Keulegan–Carpenter number has also been highlighted by Wang, Yin & Liu (2022) for the case of gravity waves. As stated previously, it is worth noting that the drag coefficient values reported by Nepf (1999) do not pertain to wave motion. Therefore, it is particularly interesting to compare the bulk drag coefficient data presented in this paper with those from Wang *et al.* (2022). In their study, Wang *et al.* (2022) conducted physical experiments using a 10-metre-long model representing a mature *Rhizophora* forest to investigate hydrodynamic characteristics and the attenuation of gravity waves. They introduced a novel parameter, i.e. a modified Keulegan–Carpenter number $KC_{r_v} = u_p T / r_v$, where $u_p = u(1 - \phi)$ is the spatially averaged flow velocity in the spaces among the stems, with u the flow velocity, $r_v = (\pi/4)((1 - \phi)/\phi)d$ a hydraulic radius related to obstacles, and T the wave period. This parameter signifies the spatially averaged flow velocity within the interstices among the stems. Finally, the authors established a correlation between the bulk drag coefficient and KC_{r_v}, producing an empirical formula for C_D. The authors observed that this formula elucidates the drag coefficient attributes of obstacles with a notably high degree of correlation.

Although the waves in this study are solitary waves, thus different from those analysed by Wang *et al.* (2022), efforts were made to compare the values of the drag coefficients from numerical and experimental runs to assess the feasibility of extending the analysis of the authors. For the configurations in this study, the computation of KC_{r_v} was performed
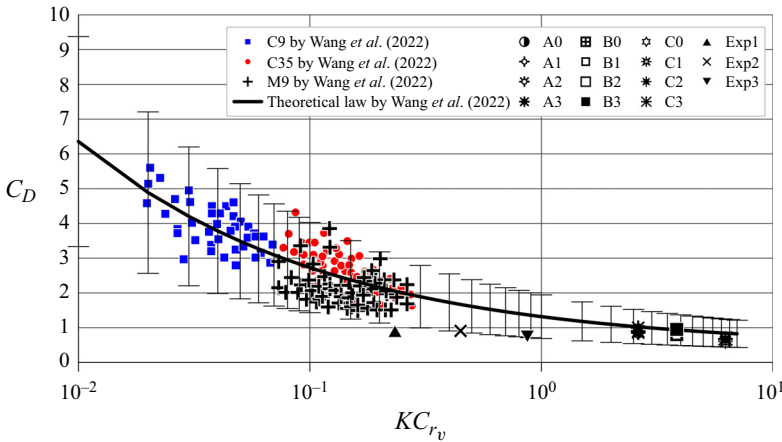
Figure 18. Relationship between KC_{r_v} and the C_D data of three vegetation models of Wang *et al.* (2022), with their theoretical curve, their proposal of a 95 % prediction band, and the data of the present study.

as follows. The value of the wave period T is based on the wavelength, calculated using (2.5), and the celerity of waves in shallow water, as proposed by Munk's theory of solitary waves (Munk 1949). The velocity values u at the passage of the soliton crest, which enabled us to compute $u_p = u(1 - \phi)$, were obtained from the numerical SPH code for the numerical configurations and experimentally for laboratory tests. Specifically, the velocity scale u for numerical configurations is approximately $O(1.5 \, \text{m s}^{-1})$, while for experimental configurations it is approximately $O(1 \, \text{m s}^{-1})$. Figure 18 illustrates that the C_D values proposed in this study align very well, even with the theoretical framework proposed by Wang *et al.* (2022), whose fitted curve has the equation

$$C_D = \left(\frac{0.77}{KC_{r_v}} \right)^{0.41} + 0.42. \tag{3.4}$$

Therefore, it can be concluded that the present study allows for extending the trend of the bulk drag coefficient by Wang *et al.* (2022), both for solitary waves alone and for solitary waves with a background current, within the limits of the experiment performed. Furthermore, it is possible to conclude that the order of magnitude of C_D is also in agreement with Nepf (1999). This is because solitary waves fall within the category of long waves, i.e. flows that, although of a wave-induced type, are those that most closely resemble stationary currents.

4. Conclusions

The present study proposes a theoretical model for the evaluation of the damping of solitary waves due to the presence of an array of emerged and submerged cylindrical obstacles on a horizontal bottom. The model was compared with the results of numerical simulations conducted with the DualSPHysics code for solitary waves for different wave parameters and stem array configurations. The results confirmed the validity of the proposed theoretical model. Experimental laboratory tests were also carried out for solitary waves with a background current, starting from the assumption that this situation appears to be the most frequent in reality. The complex experimental set-up allowed us to simultaneously evaluate the wave elevation profile in a suitable number of sections of the

channel used for three configurations of the stem array. Also in this case, the comparison of the damping of the experimental waves and that predicted by the theoretical model has provided satisfactory results. Finally, an analysis of the bulk drag coefficients C_D of solitary and regular waves in the absence of currents and of solitary waves in the presence of a background current was carried out. The results for the bulk drag coefficients of the present work are in excellent agreement with Nepf (1999). This conclusion holds both for the case of waves alone and for waves superimposed on a background current. The values slightly lower than those of Nepf (1999) for the experimental cases of solitary waves with a background current can be justified by the fact that the waves generated in the channel are subject to a reflection of the downstream gate of the channel, which leads to experimental values of wave heights greater than the theoretical ones. In the case of solitary waves with a background current, the experimental data for C_D confirm the known trend from the literature, whereby for values $ad < 0.01$, the value of C_D is almost constant. Finally, although dealing with different types of waves, efforts were made to compare the bulk drag coefficient values of the present study with those of Wang *et al.* (2022), yielding excellent results. This allowed for extending the validity of the theoretical law of Wang *et al.* (2022).

Author ORCIDs.
- Michele Mossa https://orcid.org/0000-0002-6477-8714;
- Diana De Padova https://orcid.org/0000-0002-4092-1053;
- Miguel Onorato https://orcid.org/0000-0001-9141-2147.

Appendix

The Taylor series expansion of (2.9) at $z = 0$ is given by

$$
u = C \times N \times \frac{\cosh\left(\dfrac{Mx}{h}\right)\cos\left(\dfrac{Mz}{h}\right) + 1}{\left(\cosh\left(\dfrac{Mx}{h}\right) + \cos\left(\dfrac{Mz}{h}\right)\right)^2} = C \times N \frac{\mathbb{A}\cos(\mathbb{B}z) + 1}{(\mathbb{A} + \cos(\mathbb{B}z))^2}
$$

$$
= C \times N \times \frac{1 + \mathbb{A}\sum_{k=0}^{\infty}\dfrac{(-1)^k(\mathbb{B}z)^{2k}}{(2k)!}}{\left(\mathbb{A} + \sum_{k=0}^{\infty}\dfrac{(-1)^k(\mathbb{B}z)^{2k}}{(2k)!}\right)^2}, \tag{A1}
$$

with

$$
\left.\begin{aligned}
\mathbb{A} &= \cosh\left(\frac{Mx}{h}\right), \\
\mathbb{B} &= \frac{M}{h}.
\end{aligned}\right\} \tag{A2}
$$

The Taylor series expansion of (2.9) at $z = z_0$ arrested at the second order is given by

$$
u = C \times N \times \frac{\cosh\left(\dfrac{Mx}{h}\right)\cos\left(\dfrac{Mz}{h}\right) + 1}{\left(\cosh\left(\dfrac{Mx}{h}\right) + \cos\left(\dfrac{Mz}{h}\right)\right)^2} = C \times N \frac{\mathbb{A}\cos(\mathbb{B}z) + 1}{(\mathbb{A} + \cos(\mathbb{B}z))^2}
$$

$$
= C \times N \times \left[\frac{\mathbb{A}\cos(\mathbb{B}z_0) + 1}{(\mathbb{A} + \cos(\mathbb{B}z_0))^2} - \frac{\mathbb{B}(z - z_0)\sin(\mathbb{B}z_0)\left(\mathbb{A}^2 - \mathbb{A}\cos(\mathbb{B}z_0) - 2\right)}{(\mathbb{A} + \cos(\mathbb{B}z_0))^3} \right.
$$

$$
- \frac{\mathbb{B}^2(z - z_0)^2}{2\left(\mathbb{A} + \cos(\mathbb{B}z_0)\right)^4}\left(\mathbb{A}^3\cos(\mathbb{B}z_0) + 4\mathbb{A}^2\sin^2(\mathbb{B}z_0) - \mathbb{A}\cos^3(\mathbb{B}z_0)\right.
$$

$$
\left. - 2\mathbb{A}\cos(\mathbb{B}z_0) - 2\mathbb{A}\sin^2(\mathbb{B}z_0)\cos(\mathbb{B}z_0) - 6\sin^2(\mathbb{B}z_0) - 2\cos^2(\mathbb{B}z_0)\right)
$$

$$
\left. + O\big((z - z_0)^3\big) \right]
$$

$$
= C \times N \times \left[\mathfrak{A} + \mathfrak{B}(z - z_0) + \mathfrak{C}(z - z_0)^2 + O\big((z - z_0)^3\big)\right]. \tag{A3}
$$

Generalizing, in the case of a Taylor series expansion at $z = z_0$ truncated at order $m - 1$, the remaining terms are of the order of magnitude

$$
O\big((z - z_0)^m\big), \tag{A4}
$$

therefore the convergence condition is

$$
|(z - z_0)| < 1. \tag{A5}
$$

In conclusion, integral (2.13) is

$$
\int |u^3|\,\mathrm{d}z = (C \times N)^3 \int |\mathfrak{A} + \mathfrak{B}(z - z_0) + \mathfrak{C}(z - z_0)^2|^3\,\mathrm{d}z
$$

$$
= (C \times N)^3 \times \frac{1}{140}z\left[140z^2\left(\mathfrak{A}^2\mathfrak{C} + \mathfrak{A}\big(\mathfrak{B}^2 - 6\mathfrak{B}\mathfrak{C}z_0 + 6\mathfrak{C}^2z_0^2\big)\right.\right.
$$

$$
\left. + z_0\big(-\mathfrak{B}^3 + 6\mathfrak{B}^2\mathfrak{C}z_0 - 10\mathfrak{B}\mathfrak{C}^2z_0^2 + 5\mathfrak{C}^3z_0^3\big)\right)
$$

$$
+ 84\mathfrak{C}z^4\left(\mathfrak{C}\big(\mathfrak{A} + 5\mathfrak{C}z_0^2\big) + \mathfrak{B}^2 - 5\mathfrak{B}\mathfrak{C}z_0\right)
$$

$$
+ 35z^3(\mathfrak{B} - 2\mathfrak{C}z_0)\left(2\mathfrak{C}\big(3\mathfrak{A} + 5\mathfrak{C}z_0^2\big) + \mathfrak{B}^2 - 10\mathfrak{B}\mathfrak{C}z_0\right)
$$

$$
+ 210z(\mathfrak{B} - 2\mathfrak{C}z_0)\big(\mathfrak{A} + z_0(\mathfrak{C}z_0 - \mathfrak{B})\big)^2 + 140\big(\mathfrak{A} + z_0(\mathfrak{C}z_0 - \mathfrak{B})\big)^3
$$

$$
\left. - 70\mathfrak{C}^2z^5(2\mathfrak{C}z_0 - \mathfrak{B}) + 20\mathfrak{C}^3z_0^6\right]\operatorname{sgn}\big(\mathfrak{A} + (z - z_0)(\mathfrak{B} + \mathfrak{C}(z - z_0))\big) + \text{constant}, \tag{A6}
$$

1002 A45-21

where

$$
\left.\begin{aligned}
\mathfrak{A} &= \frac{\mathbb{A}\cos(\mathbb{B}z_0) + 1}{(\mathbb{A} + \cos(\mathbb{B}z_0))^2}, \\
\mathfrak{B} &= \frac{\mathbb{B}\sin(\mathbb{B}z_0)\left(\mathbb{A}^2 - \mathbb{A}\cos(\mathbb{B}z_0) - 2\right)}{(\mathbb{A} + \cos(\mathbb{B}z_0))^3}, \\
\mathfrak{C} &= \frac{\mathbb{B}^2}{2(\mathbb{A} + \cos(\mathbb{B}z_0))^4}\left(\mathbb{A}^3\cos(\mathbb{B}z_0) + 4\mathbb{A}^2\sin^2(\mathbb{B}z_0) - \mathbb{A}\cos^3(\mathbb{B}z_0)\right. \\
&\quad \left. - 2\mathbb{A}\cos(\mathbb{B}z_0) - 2\mathbb{A}\sin^2(\mathbb{B}z_0)\cos(\mathbb{B}z_0) - 6\sin^2(\mathbb{B}z_0) - 2\cos^2(\mathbb{B}z_0)\right).
\end{aligned}\right\}
\tag{A7}
$$

Equations (A3) and (A6) enable us to calculate the wave-averaged work.

REFERENCES

ALBAYRAK, I., NIKORA, V., MILER, O. & O'HARE, M. 2011 Flow–plant interactions at a leaf scale: effects of leaf shape, serration, roughness and flexural rigidity. *Aquat. Sci.* **74** (2), 267–286.

ANTUONO, M., COLAGROSSI, A. & MARRONE, S. 2012 Numerical diffusive terms in weakly-compressible SPH schemes. *Comput. Phys. Commun.* **183**, 2570–2580.

BARILE, S., DE PADOVA, D., MOSSA, M. & SIBILLA, S. 2020 Theoretical analysis and numerical simulations of turbulent jets in a wave environment. *Phys. Fluids* **32**, 035105.

BEN MEFTAH, M. & MOSSA, M. 2016 A modified log-law of flow velocity distribution in partly obstructed open channels. *Environ. Fluid Mech.* **16**, 453–479.

BLANK, M., NAIR, P. & PÖSCHEL, T. 2024 Surface tension and wetting at free surfaces in smoothed particle hydrodynamics. *J. Fluid Mech.* **987**, A23.

BOUSSINESQ, J. 1872 Théorie des ondes et des remous qui se propagent le long d'un canal rectangulaire horizontal, en communiquant au liquide contenu dans ce canal des vitesses sensiblement pareilles de la surface au fond. *J. Math. Pures Appl.* **17**, 55–108.

CRESPO, A.J.C., DOMINGUEZ, J.M., ROGERS, B.D., GÓMEZ-GESTEIRA, M., LONGSHAW, S., CANELAS, R., VACONDIO, R., BARREIRO, A. & GARCÍA-FEAL, O. 2015 DualSPHysics: open-source parallel CFD solver based on smoothed particle hydrodynamics (SPH). *Comput. Phys. Commun.* **187**, 204–216.

DAHDOUH-GUEBAS, F. & KOEDAM, N. 1953 Coastal vegetation and the Asian Tsunami. *Science* **311** (5757), 37.

DAILY, J.M. & STEPHAN, S.C. 1953 Characteristics of the solitary wave. *Trans. Am. Soc. Civ. Engrs* **118** (1), 575–587.

DALRYMPLE, R.A. & ROGERS, B.D. 2006 Numerical modeling of water waves with the SPH method. *Coast. Engng* **53**, 141–147.

DANIELSEN, F., *et al.* 2005 The Asian Tsunami: a protective role for coastal vegetation. *Science* **310** (5748), 643.

DAS, S. & JEFFREY, R.V. 2009 Mangroves protected villages and reduced death toll during Indian super cyclone. *Proc. Natl Acad. Sci. USA* **106** (18), 7357–7360.

DE PADOVA, D., BEN MEFTAH, M., MOSSA, M. & SIBILLA, S. 2022 A multi-phase SPH simulation of hydraulic jump oscillations and local scouring processes downstream of bed sills. *Adv. Water Resour.* **159**, 104097.

DE PADOVA, D., DALRYMPLE, R.A. & MOSSA, M. 2014 Analysis of the artificial viscosity in the smoothed particle hydrodynamics modelling of regular waves. *J. Hydraul. Res.* **52**, 836–848.

DE PADOVA, D., MOSSA, M., SIBILLA, S. & TORTI, E. 2013 3D SPH modeling of hydraulic jump in a very large channel. *J. Hydraul. Res.* **51**, 158–173.

DOMÍNGUEZ, J.M., CRESPO, A.J.C. & GÓMEZ-GESTEIRA, M. 2013 Optimization strategies for CPU and GPU implementations of a smoothed particle hydrodynamics method. *Comput. Phys. Commun.* **184**, 617–627.

DOMÍNGUEZ, J.M., FOURTAKAS, G., ALTOMARE, C., CANELAS, R.B., TAFUNI, A., GARCÍA-FEAL, O., MARTÍNEZ-ESTÉVEZ, I., MOKOS, A., VACONDIO, R. & CRESPO, A.J.C. 2021 DualSPHysics: from fluid dynamics to multiphysics problems. *Comput. Part. Mech.* **9**, 867–895.

FAVRE, A. 1969 Statistical equations of turbulent gases. In *Problems of Hydrodynamics and Continuum Mechanics*, pp. 231–266. SIAM.

FULK, D.A. & QUINN, D.W. 2018 An analysis of 1-D smoothed particle hydrodynamics kernels. *J. Comput. Phys.* **126** (1), 165–180.

GIJÓN MANCHEÑO, A., JANSEN, W., UIJTTEWAAL, W., RENIERS, A.J.H.M., VAN ROOIJEN, A.A., SUZUKI, T., ETMINAN, V. & WINTERWERP, J.C. 2021 Wave transmission and drag coefficients through dense cylinder arrays: implications for designing structures for mangrove restoration. *Ecol. Engng* **165**, 106231.

GILMAN, E.L., ELLISON, J., DUKE, N.C. & FIELD, C. 2008 Threats to mangroves from climate change and adaptation options: a review. *Aquat. Bot.* **89** (2), 237–250.

GORING, D.G. 1978 Tsunamis: the propagation of long waves onto a shelf, *Keck Lab report KH-R-38*, https://doi.org/10.7907/Z9W957BN.

GOTOH, H., SHIBAHARA, T. & SAKAI, T. 2001 Sub-particle-scale turbulence model for the MPS method – Lagrangian flow model for hydraulic engineering. *Adv. Meth. Comput. Fluid Dyn.* **9**, 339–349.

HEDGES, T.S. 1987 Combinations of waves and currents: an introduction. *Proc. Inst. Civ. Engrs* **82** (3), 567–584.

HU, Z., SUZUKI, T., ZITMAN, T., UITTEWAAL, W. & STIVE, M. 2014 Laboratory study on wave dissipation by vegetation in combined current–wave flow. *Coast. Engng* **88**, 131–142.

HUANG, Z., YAO, Y., SIM, S.Y. & YAO, Y. 2011 Interaction of solitary waves with emergent, rigid vegetation. *Ocean Engng* **38** (10), 1080–1088.

KATHIRESAN, K. & RAJENDRAN, N. 2005 Coastal mangrove forests mitigated tsunami. *Estuar. Coast. Shelf Sci.* **65** (3), 601–606.

KEULEGAN, G.H. & CARPENTER, L.H. 1958 Forces on cylinders and plates in an oscillating fluid. *J. Res. Natl Bur. Stand.* **60** (5), 423–440.

KOBAYASHI, N. & LAWRENCE, A.R. 2004 Cross-shore sediment transport under breaking solitary waves. *J. Geophys. Res.* **109**, C03047.

LAUREN, N.A., IRISH, J.L. & LYNETT, P. 2009 Laboratory and numerical studies of wave damping by emergent and near-emergent wetland vegetation. *Coast. Engng* **56**, 332–340.

LIU, P. & LIU, P.L.F. 1998 Turbulence transport, vorticity dynamics, and solute mixing under plunging breaking waves in surf zone. *J. Geophys. Res. Oceans* **103**, 15677–15694.

LOSADA, I.J., MAZA, M. & LARA, J.L. 2016 A new formulation for vegetation-induced damping under combined waves and currents. *Coast. Engng* **107**, 1–13.

LOVELOCK, C.E., *et al.* 2015 The vulnerability of Indo-Pacific mangrove forests to sea-level rise. *Nature* **526** (7574), 559–563.

MADSEN, P.A., FUHRMAN, D.R. & SCHÄFFER, H.A. 2008 On the solitary wave paradigm for tsunamis. *J. Geophys. Res.*, **113**, C12012.

MAKRIS, C.V., MEMOS, C.D. & KRESTENITIS, Y.N. 2016 Numerical modeling of surf zone dynamics under weakly plunging breakers with SPH method. *Ocean Model.* **98** (1), 12–35.

MAROIS, D.E. & MITSCH, W.J. 2015 Coastal protection from tsunamis and cyclones provided by mangrove wetlands – a review. *Intl J. Biodiversity Sci.* **11** (1), 71–83.

MAZDA, Y., MAGI, M., IKEDA, Y., KUROKAWA, T. & ASANO, T. 2006 Wave reduction in a mangrove forest dominated by *Sonneratia sp*. *Wetlands Ecol. Manage.* **14**, 365–378.

MAZDA, Y., MAGI, M., KOGO, M. & HONG, P.N. 1997 Mangroves as a coastal protection from waves in the Tong King delta, Vietnam. *Mangroves Salt Marshes* **1**, 127–135.

MCCOWAN, J. 1891 On the solitary wave. *Lond. Edinb. Dubl. Phil. Mag. J. Sci.* **5** (32), 45–58.

MEI, C.C., CHAN, I.-C., LIU, P.L.-F., HUANG, Z. & ZHANG, W. 2011 Long waves through emergent coastal vegetation. *J. Fluid Mech.* **687**, 461–491.

MENDEZ, F.J. & LOSADA, I.J. 2004 An empirical model to estimate the propagation of random breaking and nonbreaking waves over vegetation fields. *Coast. Engng* **51**, 103–118.

MOLTENI, D. & COLAGROSSI, A. 1985 A simple procedure to improve the pressure evaluation in hydrodynamic context using the SPH. *Comput. Phys. Commun.* **180**, 861–872.

MONAGHAN, J.J. & LATTANZIO, J.C. 1985 A refined particle method for astrophysical problems. *Astron. Astrophys.* **149**, 135–143.

MOSSA, M., BEN MEFTAH, M., DE SERIO, F. & NEPF, H.M. 2017 How vegetation in flows modifies the turbulent mixing and spreading of jets. *Sci. Rep.* **7**, 6587.

MOSSA, M. & DE SERIO, F. 2016 Rethinking the process of detrainment: jets in obstructed natural flows. *Sci. Rep.* **6**, 39103.

MOSSA, M., GOLDSHMID, R.H., LIBERZON, D., NEGRETTI, M.E., SOMMERIA, J., TERMINI, D. & DE SERIO, F. 2021 Quasi-geostrophic jet-like flow with obstructions. *J. Fluid Mech.* **921**, A12.

MUNK, W.H. 1949 The solitary wave theory and its application to surf problems. *Ann. N.Y. Acad. Sci.* **51**, 376–462.

NEPF, H.M. 1999 Turbulence and diffusion in flow through emergent vegetation. *Water Resour. Res.* **35** (2), 479–489.

PATEL, D.M., PATEL, V.M., KATRIYA, B. & PATEL, K.A. 2014 Performance of mangrove in tsunami resistance. *Intl J. Emerg. Technol. Res.* **1** (3), 29–32.

RUSSELL, J.S. 1845 Report on waves. In *Proceedings of the 14th Meeting of the British Association for the Advancement of Science, York, September 1844 (London 1845), Plates XLVII-LVII*, pp. 90–311.

SHAO, S. & LO, E.Y.M. 2003 Incompressible SPH method for simulating Newtonian and non-Newtonian flows with a free surface. *Adv. Water Resour.* **26** (7), 787–800.

SYNOLAKIS, C.E., BERNARD, E.N., TITOV, V.V., KÂNOGLU, U. & GONZÁLEZ, F.I. 2007 Standards, criteria and procedures for NOAA evaluation of tsunami numerical models. In *NOAA Technical Memorandum*, OAR PMEL, vol. 135, p. 55.

TANINO, Y. & NEPF, H.M. 2007 Lateral dispersion in random cylinder arrays at high Reynolds number. *J. Fluid Mech.* **600**, 339–371.

VIOLEAU, D. 2012 *Fluid Mechanics and the SPH Method: Theory and Applications*. Oxford University Press.

WANG, Y., YIN, Z. & LIU, Y. 2022 Experimental investigation of wave attenuation and bulk drag coefficient in mangrove forest with complex root morphology. *Appl. Ocean Res.* **118**, 102974.

WHITE, B.L. & NEPF, H.M. 2007 Shear instability and coherent structures in shallow flow adjacent to a porous layer. *J. Fluid Mech.* **593**, 1–32.

YEH, H., LIU, P.L.-F., BRIGGS, M. & SYNOLAKIS, C.E. 1994 Propagation and amplification of tsunamis at coastal boundaries. *Nature* **37226**, 353–355.

ZHANG, H. & NEPF, X. 2022 Reconfiguration of and drag on marsh plants in combined waves and current. *J. Fluids Struct.* **110**, 103539.

ZHANG, J., ZHENG, J., JENG, D.S. & GUO, Y. 2015 Numerical simulation of solitary-wave propagation over a steady current. *ASCE J. Waterway Port Coastal Ocean Engng* **141** (3), 04014041.